Earth and Planetary Science Letters 594 (2022) 117743

Contents lists available at ScienceDirect

Earth and Planetary Science Letters

www.elsevier.com/locate/epsl

Ca-isotopes as a robust tracer of magmatic differentiation

Hairuo Fu [a,*], Stein B. Jacobsen [a], Bjørn T. Larsen [b], Zachary T. Eriksen [a]

[a] Department of Earth and Planetary Sciences, Harvard University, MA 02138, USA
[b] Department of Geosciences and CEED, University of Oslo, P.O. Box 1047 Blindern, N-0316 Oslo, Norway

ARTICLE INFO

Article history:
Received 31 March 2022
Received in revised form 3 July 2022
Accepted 19 July 2022
Available online 3 August 2022
Editor: R. Dasgupta

Keywords:
Ca isotopes
isotope fractionation
magmatic evolution
planetary differentiation

ABSTRACT

The large mass difference (~10%) between the two most abundant isotopes of calcium, ^{40}Ca and ^{44}Ca, gives Ca great potential in tracking mass-dependent fractionation during magmatic processes. Resolvable Ca-isotope fractionation during fractional crystallization of magma, particularly by feldspar in evolved melts, has been theoretically inferred but not robustly tested in nature. To further explore the effects of magmatic differentiation on Ca-isotope systematics, we studied the late-Permian alkaline igneous suite of the Øyangen Caldera, Oslo Rift, Norway, consisting of volcanic and intrusive units ranging from basanitic to rhyolitic compositions. Major and trace element variations and modeling demonstrate that the main series of samples ($N = 21$), including basanites, ring-dyke syenites, and central-dome syenites, likely documents a co-genetic and closed-system fractional crystallization sequence. Our data show minimal $\delta^{44/40}$Ca variation (< 0.05‰) in the intermediate magma and a marked increase in $\delta^{44/40}$Ca in the felsic magma of the Øyangen Caldera (from 0.62 ± 0.02‰ to 1.15 ± 0.03‰ relative to Ca standard, SRM915a). The systematic increase is best explained by equilibrium isotopic fractionation dominated by alkali feldspar in the fractionating mineral assemblage. This is further supported by strong correlations between $\delta^{44/40}$Ca, CaO, and Eu/Eu* in the main-series samples. Implementing a Monte Carlo approach, isotopic modeling of the liquid line of descent using Rayleigh fractionation is highly consistent with the observed Ca-isotope evolution. For the first time, we confirm prominent Ca stable isotope fractionation in felsic-stage differentiation of alkaline magma and constrain the isotope fractionation factors of plagioclase and K-feldspar. Integrated with extant estimations on mineral fractionation factors from the literature, our results suggest increasing fractionation effects of rock-forming minerals with decreasing Ca content. The affirmation of significant Ca-isotope fractionation in alkaline magma by feldspar empowers the application of Ca as a versatile tracer of crustal evolution, allowing further tests in other magmatic conditions across various planetary objects.

1. Introduction

Mass-dependent fractionation of stable isotopes opens a new window in our understanding of magmatic evolution. Although previously perceived as negligible in high-temperature igneous processes (Johnson et al., 2004; Teng et al., 2017), recent advances in high-precision isotope measurements have resolved significant mass fractionation of non-traditional stable isotopes (e.g., K, Mg, Si, Ca, and Fe) between igneous rocks of different petrogenesis. Such discoveries were attributed to a variety of magmatic processes, such as partial melting, mantle heterogeneity, and igneous differentiation (Huang et al., 2010, 2011; Kang et al., 2017; Schiller et al., 2017; Zhang et al., 2018; Brewer et al., 2018; Wang (王阳) et al., 2019; Valdes et al., 2019; Amsellem et al., 2020; Sun et al., 2021; Zhu et al., 2021; Eriksen and Jacobsen, 2022). Calcium is the fifth most abundant element in Earth's crust and has six stable isotopes (^{40}Ca, ^{42}Ca, ^{43}Ca, ^{44}Ca, ^{46}Ca, and ^{48}Ca) that exhibit the third-largest relative mass variation (20%) after H and He. The ~10% mass difference between the two most abundant isotopes, ^{40}Ca and ^{44}Ca, makes Ca a valuable candidate for tracking mass fractionation during magmatic differentiation.

Calcium-isotope variation during partial melting of mantle rocks (olivine, pyroxene, and garnet dominant) has been extensively studied (e.g., Huang et al., 2010; Kang et al., 2017; Chen et al., 2019), however, Ca-isotope fractionation in crustal magmatic processes (feldspar dominant), especially during fractional crystallization, has remained obscure and controversial. Zhang et al. (2018) analyzed a consecutive sequence of basalts from the Kilauea Iki lava lake, Hawaii, showing no measurable variations of ^{44}Ca/^{40}Ca (<0.07‰) during crystallization. These results, however, only apply to the mafic to intermediate range of compositions.

* Corresponding author.
E-mail address: hairuo.fu@g.harvard.edu (H. Fu).

https://doi.org/10.1016/j.epsl.2022.117743
0012-821X/

In contrast, a study of an Archaean ultramafic-mafic-anorthosite igneous complex from the West Africa Craton reported extreme $^{44}Ca/^{40}Ca$ isotopic fractionation (~3.2‰) interpreted to be the result of fractional crystallization (Valdes et al., 2019). Nevertheless, the Ca-isotope variation observed from the samples in Valdes et al. (2019) may instead reflect inter-mineral diffusion during metamorphism of the protoliths (peak *P-T* conditions of 900 °C and 5 kbar) (Valdes et al., 2019; Antonelli and Simon, 2020). More recently, Zhu et al. (2021) found a ~0.2‰ change in $^{44}Ca/^{40}Ca$ among the andesitic–rhyolitic volcanic glasses from the eastern Manus Basin, southwestern Pacific. However, their implications hinge on relatively large analytical uncertainties and the resulting inadequate resolution between equilibrium fractionation and kinetic isotope effects.

Therefore, to robustly understand how Ca isotopes fractionate during fractional crystallization necessitates high-resolution surveys of a co-genetic and unaltered magma sequence. We targeted the late-Permian alkaline igneous suite of the Øyangen Caldera, Oslo Rift, southern Norway, for a case study that recorded a continuous closed-system fractional crystallization series. Ca-isotope data robustly depict prominent $^{44}Ca/^{40}Ca$ variation (~0.53‰) in the evolved felsic magma (trachytic–rhyolitic), contrasting with minimal fractionation (<0.05‰) in the intermediate magma (trachyandesitic). By comparing isotope data with isotopic modeling, we found that the marked Ca-isotope fractionation is most likely explained by Rayleigh (equilibrium) isotopic fractionation, with a dominant control by feldspar. We also quantified the Ca-isotope fractionation factors of K-feldspar for the first time. The new findings underscore the enhanced power of Ca stable isotopes in tracing magma differentiation and crustal evolution facilitated by our high-precision measurements.

2. Geological settings and samples

The Øyangen Caldera in the Oslo Rift developed in the late Permian (ca. 273 Ma, U-Pb thermal ionization mass spectrometry zircon ages) (Corfu and Larsen, 2020) during a prolonged period of rift-related magmatic activity associated with the Oslo Rift from ca. 300–260 Ma (Fig. 1) (Corfu and Dahlgren, 2008; Corfu and Larsen, 2020). The Oslo Rift is located in the foreland of the Variscan Orogen, formed by NW-SE lithospheric extension associated with accumulated tectonic stress during the Laurasia-Gondwana collision (Neumann et al., 2004). It has preserved a series of rift-related sedimentary and igneous rocks, among which the Øyangen Caldera formed in its late-stage development (Fig. 1A) (Neumann et al., 1992; Larsen et al., 2008; Corfu and Larsen, 2020). The basement on both sides of this part of the Oslo Rift consists of high-grade metamorphic rocks (ca. 1.64–1.52 Ga) (Lamminen et al., 2011). This basement is overlain by a few hundred meters to a kilometer of Cambrian to Silurian sediments adjacent to the Øyangen Caldera complex (Fig. 1A). Basaltic lavas of the central volcano marked the onset of Øyangen Caldera magmatism. Caldera collapse followed with the emplacement of ring dykes and central domes and ignimbrite eruptions toward more evolved trachytic–rhyolitic magma compositions (Larsen et al., 2008). For calderas, access to deep-seated magma is assumed to be cut off before the caldera collapse (e.g., Cashman and Giordano, 2014), favoring a closed-system fractional crystallization origin of the igneous suite. Well-preserved remnants of the caldera complex in the area enable comprehensive petrological and geochemical characterization with clear geological context.

To constrain the extent of magma evolution, 21 representative samples collected from the Øyangen Caldera were selected for elemental and isotopic analysis, including 2 basanites, 12 syenites (8 from coarse-grained ring dykes and 4 from fine-grained central domes), and 7 trachytic–rhyolitic ignimbrites (6 trachytes and 1 rhyolite) (Fig. 1A, Table 1). The basanites are mainly comprised of olivine and clinopyroxene with minimal plagioclase. The syenites and trachytic–rhyolitic ignimbrites predominantly consist of feldspar. The ring-dyke syenites contain mostly anorthoclase, while the central-dome syenites and trachytic–rhyolitic ignimbrites contain primarily potassium feldspar. The main-series magma consists of basanites, ring-dyke syenites, and central-dome syenites, complemented by eruptive trachytic–rhyolitic ignimbrites with a more complicated petrogenesis.

3. Methods

3.1. Sample preparation

All whole-rock samples were ground into fine powders, from which we weighed ~50 mg for each to ensure homogeneous bulk compositions. The samples were then processed through standard silicate dissolution (Supplementary Material: Section 1). Major and trace element analyses were performed on a Thermo Scientific iCAP-TQ quadrupole inductively coupled plasma mass spectrometer (ICP-MS) in the Harvard University isotope geochemistry and cosmochemistry laboratory. Dilute HNO_3 (~2%) spiked with 10 parts per billion (ppb) indium, for internal instrumental drift correction, was added into sample aliquots to make final solutions for elemental analysis. Three standard solutions BCR-1, BHVO-1, and AGV-1 were measured to define calibration curves to determine the elemental concentrations of the samples. Major elements of mineral phenocrysts separated from the samples, including clinopyroxene, amphibole, and feldspar, were analyzed by X-ray fluorescence (XRF) at the University of Oslo, Norway.

We adapted a modified Ca separation technique following Feng et al. (2018). For calcium-rich samples (CaO wt.% > 1 — basanites and primitive ring-dyke syenites), we loaded sample aliquots containing 40 µg Ca in 4 N HNO_3 onto PFA microcolumns packed with Eichrom DGA spec normal extraction resin (2.4 mm inner diameter, 54 mm height, ~250 µL bed volume). We accelerated the extraction process with a modified Eichrom vacuum box, setting a stable flow rate at ~1 mL/5 minutes. Ten bed volumes of 0.1 N HCl (2.5 mL) followed by five bed volumes of 4 N HNO_3 (1.25 mL) were used to clean and condition the column before sample loading. We eluted major elements with a total of 8 mL 4 N HNO_3 and collected pure Ca solutions in 4 mL Milli-Q purified deionized water (for a representative column calibration curve see Fig. S4). Separated Ca solutions were then evaporated to dryness on a hot plate and were redissolved in 2% HNO_3 to make final Ca stock solutions.

We found that with very low Ca concentrations [CaO (wt.%) < 1%], separation on the DGA micro-columns often led to impure Ca solutions (Ca purity < 99%), which are not ideal for isotopic measurements with the Nu Sapphire multicollector (MC) ICP-MS due to potential matrix effects. Therefore, to first concentrate Ca in the low-Ca samples (evolved syenites from ring dykes and central domes and trachytic–rhyolitic ignimbrites), they were pre-processed through a 17-cm quartz glass column packed with BioRad AG50W-X8, 100-200 mesh, cation exchange resin eluting with 1.5 N and 2.5 N HCl (method modified from Tera et al., 1970) (for a representative column calibration curve see Fig. S5). A PFA teflon column (4.0 mm inner diameter, 40 mm height, ~500 µL bed volume) packed with Eichrom DGA spec normal extraction resin was used as a second step to purify the Ca, eluting major elements with 2 mL 4 N HNO_3 and collecting Ca in 5 mL Milli-Q water. The preliminary separates were then dried and loaded onto the 54 mm PFA teflon microcolumns for final Ca purification. Testing of this method demonstrates that it introduces no additional Ca-isotope fractionation (Supplementary Material: Section 2.1). We

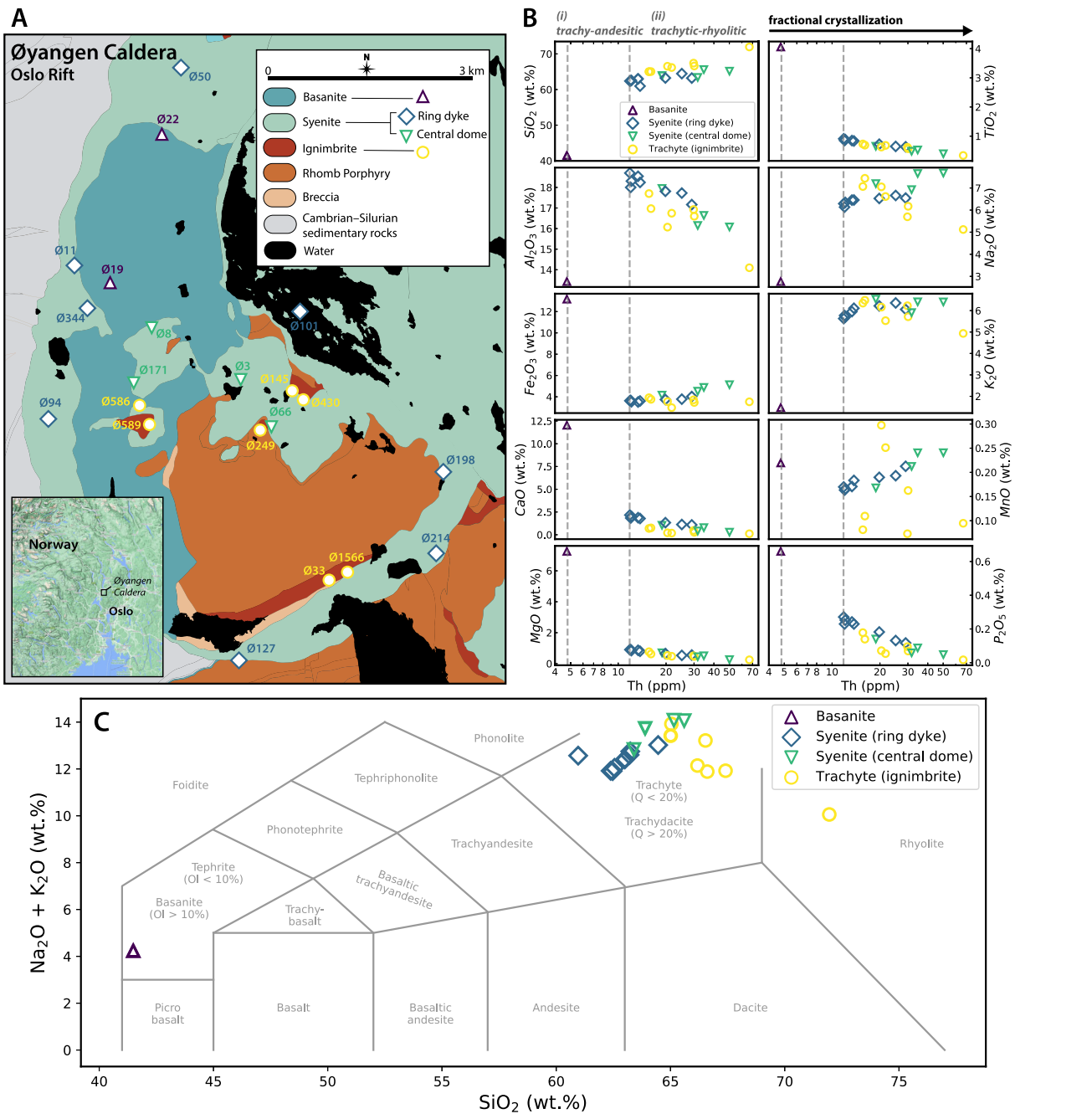

Fig. 1. Sampling locations and major element variations of the Øyangen Caldera, Oslo Rift, Norway. (A) simplified geological map of the late-Permian Øyangen Caldera (ca. 273 Ma). (B) Major element vs. Th diagrams showing variations throughout fractional crystallization of the magma. (C) Total Alkali versus Silica classification of the samples.

tested all separated Ca solutions on our iCAP-TQ quadrupole ICP-MS, ensuring Ca purity [Ca (wt.)/total mass] > 99% for all sample solutions.

3.2. Ca isotope measurements

We measured Ca isotope ratios with a Nu Sapphire MC-ICP-MS (serial no. SP001) in the Harvard University isotope geochemistry and cosmochemistry laboratory. The Nu Sapphire (MC) ICP-MS features a low-energy ion path with a hexapole collision/reaction cell that circumvents the $^{40}Ar^{+}$ interference on mass 40, permitting direct measurement of ^{40}Ca relative to other Ca isotopes. We used 2% HNO_3 to dilute purified Ca solutions to ~350 ppb for analysis. An Apex Omega Desolvating Nebulizer introduced the Ca solutions to the plasma torch. After fine-tuning, peak ^{40}Ca signal reached up to ~300 V. We implemented a sample-standard bracketing approach to correct for instrumental mass fractionation and internal drift throughout data acquisition, using our in-house laboratory standard, a very high purity Ca solution from Inorganic Ventures (CaIV-1). Each run included 5 repetitive measurements for each sample. We repeated runs for most of the samples on multiple days, obtaining 10 to 20 total measurements. We acquired an average of ~0.022‰ internal precision (two standard errors) for $^{44}Ca/^{40}Ca$ measurements (Supplementary Material: Section 2.1).

We express stable Ca isotope data using δ-notation:

$$\delta^{44/i}\mathrm{Ca}(‰) = [(^{44}\mathrm{Ca}/^{i}\mathrm{Ca})_{\mathrm{sample}}/(^{44}\mathrm{Ca}/^{i}\mathrm{Ca})_{\mathrm{standard}} - 1] \times 1{,}000 \quad (1)$$

where i is the Ca isotope mass 40 or 42. Unless specified as $\delta^{44/40}Ca_{CaIV}$, we report $\delta^{44/i}Ca$ values relative to standard SRM915a. The $\delta^{44/40}Ca$ value of SRM915a relative to CaIV-1 ($\delta^{44/40}Ca_{CaIV}$) has been determined in the lab with external reproducibility of 0.011‰ over the past two years (Fig. S1, Table S4). As such, the minimal uncertainty is neglected when converting $\delta^{44/40}Ca_{CaIV}$ to $\delta^{44/40}Ca_{SRM915a}$. We estimated a ~0.028‰ external reproducibility for the $\delta^{44/40}Ca$ data. See Supplementary Material: Section 2 for more details on mass spectrometry.

4. Results

4.1. Major and trace elements

Major and trace element data for whole-rock samples are reported in Table S1. We illustrate major element variability relative to Th, a highly incompatible trace element in major rock-forming minerals (partition coefficient, the ratio of concentrations of an element between a mineral and the melt, close to zero, $D^{Th} \approx 0$) (Allègre et al., 1977) (Fig. 1B). Highly incompatible elements concentrate in the melt as the magma crystallizes because they do not easily fit into the crystal lattices of commonly fractionating minerals. Therefore, highly incompatible elements serve as robust indexes of igneous differentiation. Using major element concentrations, we subdivide the Øyangen Caldera samples into two main crystallization stages – (1) the trachy-andesitic stage, ranging from the evolved basanite (O-19) to the most primitive ring-dyke syenite (O-214) (intermediate stage), and (2) the trachytic–rhyolitic stage, ranging from the most primitive ring-dyke syenite to the most evolved rhyolitic ignimbrite (O-249) (felsic stage) (Fig. 1B). As Th concentrates in the residual melt with increasing magma solidification, (1) SiO_2 increases while MgO and CaO decrease, (2) Al_2O_3 elevates in the trachy-andesitic melts but starts to decline in the trachytic–rhyolitic melts (3) Na_2O and K_2O remain incompatible until the magma becomes felsic, and (4) there is a gradual depletion of TiO_2 and P_2O_5 and mild variations in Fe_2O_3 and MnO in the felsic stage, reflecting fractionation of accessory minerals like ilmenite, titano-magnetite, and apatite (Fig. 1B). Feldspar compositions are plotted in Fig. 5C (Table S2), indicating that the ring-dyke syenites reflect an anorthoclase component while the central-dome syenites and trachytic–rhyolitic ignimbrites consist of mainly potassium feldspar.

Key trace elements in assessing the crystallization sequence are presented in Figs. 2 & 3. Figs. 2A and 2B show excellent linear correlations between highly incompatible elements in a log-log scale (Be, Th, and U), reflecting nearly constant D throughout the magma crystallization (Allègre et al., 1977). Fig. 2E plots the Bulk Silicate Earth (BSE) (McDonough and Sun, 1995) normalized Rare Earth Element (REE) pattern, featuring a growing negative Eu anomaly and increasing concentrations of REEs as the magma differentiates. Variation of CaO, Sr, Ba, and Eu as a function of degree of crystallization are shown in Fig. 3, compared to our elemental modeling results (see text in Discussion 5.1).

4.2. Ca-isotope compositions

$\delta^{44/40}Ca$ versus $\delta^{44/42}Ca$ is shown in Fig. 4, plotted together with theoretical mass-dependent fractionation lines under equilibrium and kinetic modes. The total range of $\delta^{44/40}Ca$ values is 0.23‰ to 0.88‰ (Fig. 4B). Intermediate and felsic samples deviate significantly from the mass fractionation relationships, with lighter $\delta^{44/40}Ca$ than is predicted (Fig. 4B). They show increasing departures from the expected relationship with increasing K/Ca ratios, corresponding to ring-dyke syenites, central-dome syenites, and trachytic–rhyolitic ignimbrites, respectively (Fig. 4B). This suggests that the observed displacements are likely due to ^{40}Ca ingrowth via the decay of ^{40}K to ^{40}Ca (half-life of 1.25 billion years). Using the measured K/Ca ratio for each sample (~2% external reproducibility) and the age of the rocks (ca. 273 Ma, Corfu and Larsen, 2020), we quantify the radiogenic excess of ^{40}Ca with the fractionation corrected $^{40}Ca/^{44}Ca$ ratio, expressed as $\varepsilon^{40/44}Ca$ relative to the fractionation corrected terrestrial $^{40}Ca/^{44}Ca$ ratio of 47.153 (Russell et al., 1978), using equation (2):

$$\varepsilon^{40/44}Ca = [(^{40}Ca/^{44}Ca)_{sample\ (frac\text{-}corr)}/(^{40}Ca/^{44}Ca)_{terrestrial\ (frac\text{-}corr)} - 1] \times 10{,}000 \quad (2)$$

$\varepsilon^{40/44}Ca$ is then used to correct for radiogenic ingrowth in the $\delta^{44/40}Ca$ values of our samples (Fig. 4A) (Supplementary Material: Section 5). After applying the age correction, all samples plot along the mass fractionation lines within analytical uncertainty except sample O-1566 (Fig. 4B). Therefore, radiogenic ingrowth of ^{40}Ca is the primary cause of the scatter about the expected mass-dependent fractionation line.

The radiogenic-excess-corrected $\delta^{44/40}Ca$ data exhibit a total of ~0.68‰ variation that ranges from 0.47 ± 0.02‰ to 1.15 ± 0.03‰ (Table 1). The basanites have similar $\delta^{44/40}Ca$ values; $\delta^{44/40}Ca$ increases systematically from primitive ring-dyke syenites to differentiated central-dome syenites; while the trachytic–rhyolitic ignimbrites scatter over a large variability (Fig. 4B) (Table 1).

5. Discussion

5.1. Co-genetic fractional crystallization of the Øyangen Caldera

Major element variations as a function of Th are consistent with a fractional crystallization origin for the Øyangen Caldera (Fig. 1B), in which the intermediate stage is dominated by fractionation of clinopyroxene + amphibole + plagioclase and the felsic stage is controlled by fractionation of alkali feldspar + clinopyroxene. Such a change in the crystallizing mineral assemblage agrees with the mineral analyses (Table S2).

Correlations between highly incompatible elements also support a fractional crystallization sequence of the Øyangen Caldera. Excellent linear relationships ($R^2 > 0.9$) and slopes ≈ 1 between Be, Th, and U in log-log plots (Fig. 2A&B) are distinctive manifestations of a co-genetic magma series formed by closed-system fractional crystallization (Allègre et al., 1977). The evolution of elemental concentrations following fractional crystallization gives:

$$\frac{C_m^i}{C_T^i} = F^{(D^i - 1)} \quad (3)$$

Where C_m^i is the concentration of element i in the remaining melt; C_T^i is the concentration of i in the primary magma; D^i is the partition coefficient; F is the residual melt fraction. For a highly incompatible element ($D \approx 0$), F associated with a sample can be calculated using the elemental concentration in the parental magma (C_T^i) and in each individual sample (Allègre et al., 1977):

$$F = C_T^i / C_{sample}^i \quad (4)$$

Here we used the evolved basanite O-19 for the parental magma composition (C_T^i) to study the intermediate and felsic magmatic differentiation. We computed F independently using Be, U, and Th and averaged the results to obtain a mean F-value, which we converted to the degree of crystallization, defined here as 1-F (Table 1, Table S1). We also modeled the liquid line of descent of the

Table 1
Ca isotope compositions and magmatic context for the samples.

Sample	$^{44}Ca/^{40}Ca$				$^{44}Ca/^{42}Ca$			CaO	Eu/Eu*	Degree of crystallization	*T*	K/Ca	$\varepsilon^{40/44}Ca$	*n*
	$\delta^{44/40}Ca_{CaIV\ (no\ corr.)}$	$\delta^{44/40}Ca_{SRM915a\ (no\ corr.)}$	$\delta^{44/40}Ca_{SRM915a\ (corr.)}$	± 2SE	$\delta^{44/42}Ca_{CaIV}$	$\delta^{44/42}Ca_{SRM915a}$	± 2SE	(wt.%)		(%)	(°C)	(wt.)		
Basanite														
O-22	−0.062	0.655	0.659	0.019	−0.043	0.292	0.015	11.3	1.01	-	-	0.2	0.04	20
O-19	−0.052	0.665	0.667	0.021	−0.023	0.312	0.020	12.0	0.99	0.0	1120	0.2	0.03	15
Syenite (ring dyke)														
O-214	−0.160	0.557	0.615	0.023	−0.031	0.304	0.022	1.8	1.12	54.0	1010	3.3	0.58	15
O-198	−0.106	0.611	0.657	0.027	−0.036	0.299	0.023	2.2	1.31	54.6	1008	2.6	0.46	15
O-101	−0.090	0.627	0.678	0.028	−0.017	0.318	0.014	2.0	1.22	58.7	991	2.9	0.52	15
O-127	−0.092	0.625	0.683	0.025	−0.001	0.334	0.019	1.9	1.15	61.6	978	3.3	0.58	15
O-11	−0.038	0.679	0.744	0.022	0.026	0.361	0.017	1.8	1.06	62.8	972	3.6	0.65	15
O-50	0.040	0.757	0.852	0.023	0.076	0.411	0.026	1.3	0.62	72.0	929	5.4	0.96	15
O-344	−0.035	0.682	0.800	0.017	0.040	0.375	0.020	1.1	0.40	79.0	893	6.6	1.18	15
O-94	0.036	0.753	0.875	0.022	0.064	0.399	0.012	1.1	0.29	81.8	878	6.8	1.22	15
Syenite (central dome)														
O-8	−0.094	0.623	0.725	0.039	−0.012	0.323	0.029	1.0	0.68	70.8	934	5.7	1.02	15
O-66	0.162	0.879	1.047	0.034	0.129	0.464	0.033	0.4	0.25	83.3	870	9.4	1.67	15
O-171	−0.016	0.701	0.847	0.030	0.054	0.389	0.018	0.8	0.23	83.9	867	8.2	1.46	15
O-3	0.133	0.850	1.149	0.027	0.201	0.536	0.018	0.3	0.13	88.5	842	16.8	2.99	15
Trachytic-rhyolitic ignimbrite														
O-430	−0.044	0.673	0.803	0.047	0.006	0.341	0.024	0.8	0.70	65.7	959	7.3	1.30	15
O-586	−0.395	0.322	0.468	0.022	−0.091	0.244	0.027	0.7	0.76	65.7	959	8.2	1.46	10
O-33	−0.103	0.614	1.053	0.017	0.187	0.522	0.027	0.2	0.60	71.8	930	24.7	4.39	15
O-1566	0.121	0.838	1.152	0.028	0.155	0.490	0.019	0.2	0.60	72.3	927	17.7	3.15	10
O-145	−0.212	0.505	0.803	0.017	0.032	0.367	0.025	0.5	0.25	80.9	883	16.8	2.98	15
O-589	0.026	0.743	1.085	0.024	0.185	0.520	0.025	0.3	0.38	81.0	882	19.3	3.42	15
O-249	−0.485	0.232	0.997	0.026	0.118	0.453	0.021	0.1	0.07	90.7	829	43.0	7.65	15

Notes: (corr.)/(no corr.) — corrected/not corrected for radiogenic excess of ^{40}Ca. *n* is the number of replicate measurements. Crystallization temperature, *T* (°C), is determined from the fitting of *T* (°C) as a fuction of degree of crystallization (Fig. 2D). 2SE represents two standard errors of the means. An about 2% error in the measured K/Ca (wt.) has been propagated to obtain the 2SE of $\delta^{44/40}Ca$ data.

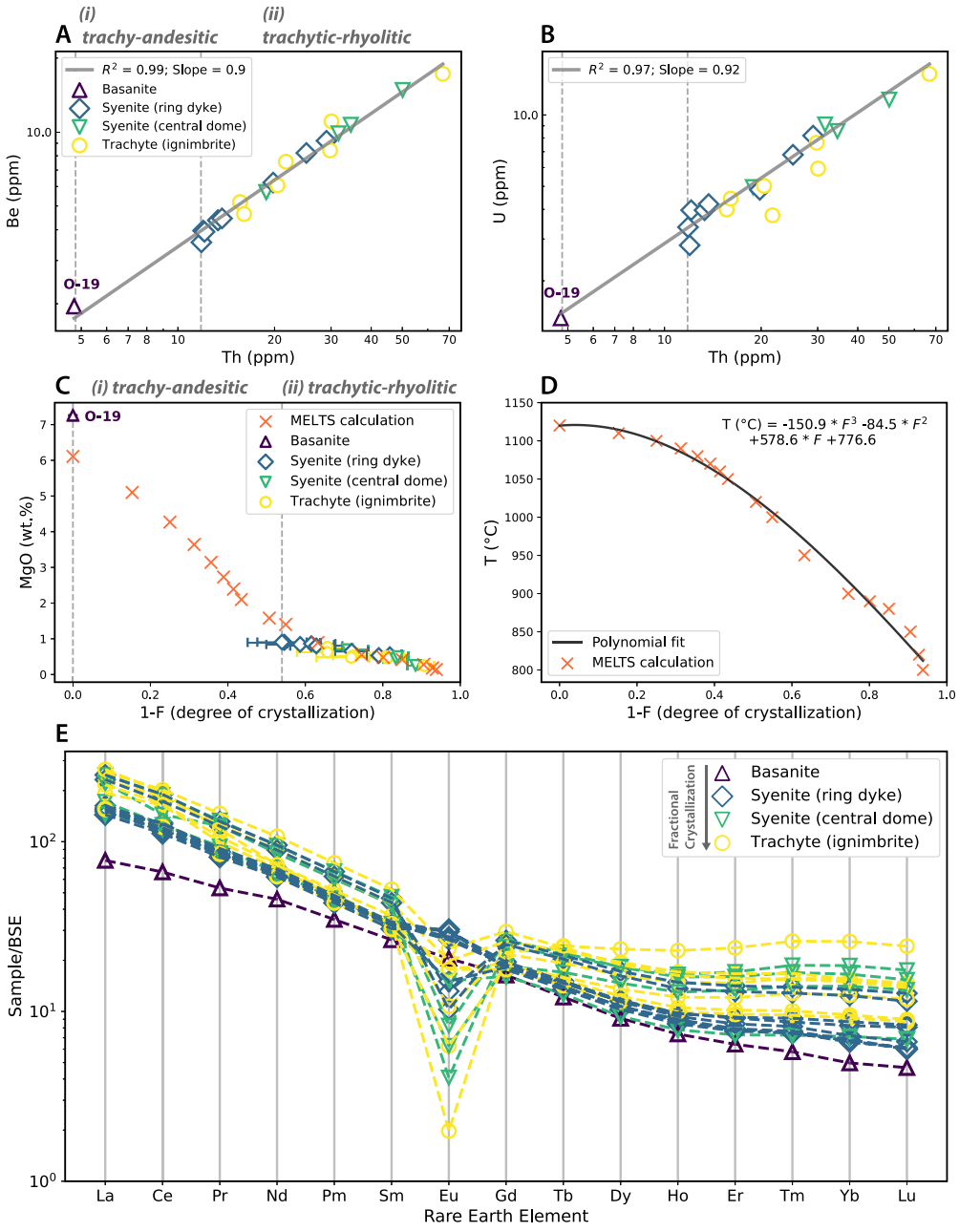

Fig. 2. Trace element variations and calculation of residual melt fraction (F). (A) & (B) Highly incompatible elements expressed on a log-log scale exhibit excellent linear correlations for the main-series samples (basanites, ring-dyke syenites, and central-dome syenites), suggesting a co-genetic closed-system fractional crystallization sequence. This enables using Be, U, and Th (Table S1) to independently calculate the residual melt fraction (F). (C) Consistent variation of MgO and 1-F between the MELTS modeling results and our independent estimate of 1-F. Our estimates of degree of crystallization (1-F) are computed by applying Be, U, and Th concentrations to equation (4). (D) A polynomial fit to T (°C) vs. 1-F that solves for magma crystallization temperature as a function of degree of crystallization. (E) Bulk Silicate Earth (BSE)-normalized REE patterns (BSE values from McDonough and Sun, 1995).

Øyangen Caldera using the Rhyolite-MELTS thermodynamic program (Gualda et al., 2012). For MELTS modeling, we implemented a fractional crystallization model and used O-22 (the most primitive basanite) as the primary magma composition (Supplementary Material: Section 3). Fig. 2C shows the high consistency of MgO vs. 1-F between the MELTS calculation and our estimate of 1-F using highly incompatible elements, substantiating that the samples document a closed-system fractional crystallization sequence. Therefore, the crystallization temperatures of the samples can be constrained by fitting temperature as a function of F from the MELTS results (Fig. 2D).

To estimate the proportions of fractionating minerals in individual crystallization stages, we implemented a weighted-least-squares method (Wright and Doherty, 1970) with our measured major element concentrations for mineral phenocrysts (for results see Fig. 3A and Table S3) (Supplementary Material: Section 4). We also determined the mineral proportions for the crystallization stages of the syenites from ring dykes and central domes independently (Fig. 5D). For robustness, we tested our crystallization model with trace element modeling assuming fractional crystallization [equation (3)] and compare it with equilibrium crystallization, a presumed less likely explanation for the caldera magma chamber (e.g., Cashman and Giordano, 2014; Gavrilenko et al., 2016):

$$\frac{C_m^i}{C_T^i} = \left[F + D^i(1-F)\right]^{-1} \tag{5}$$

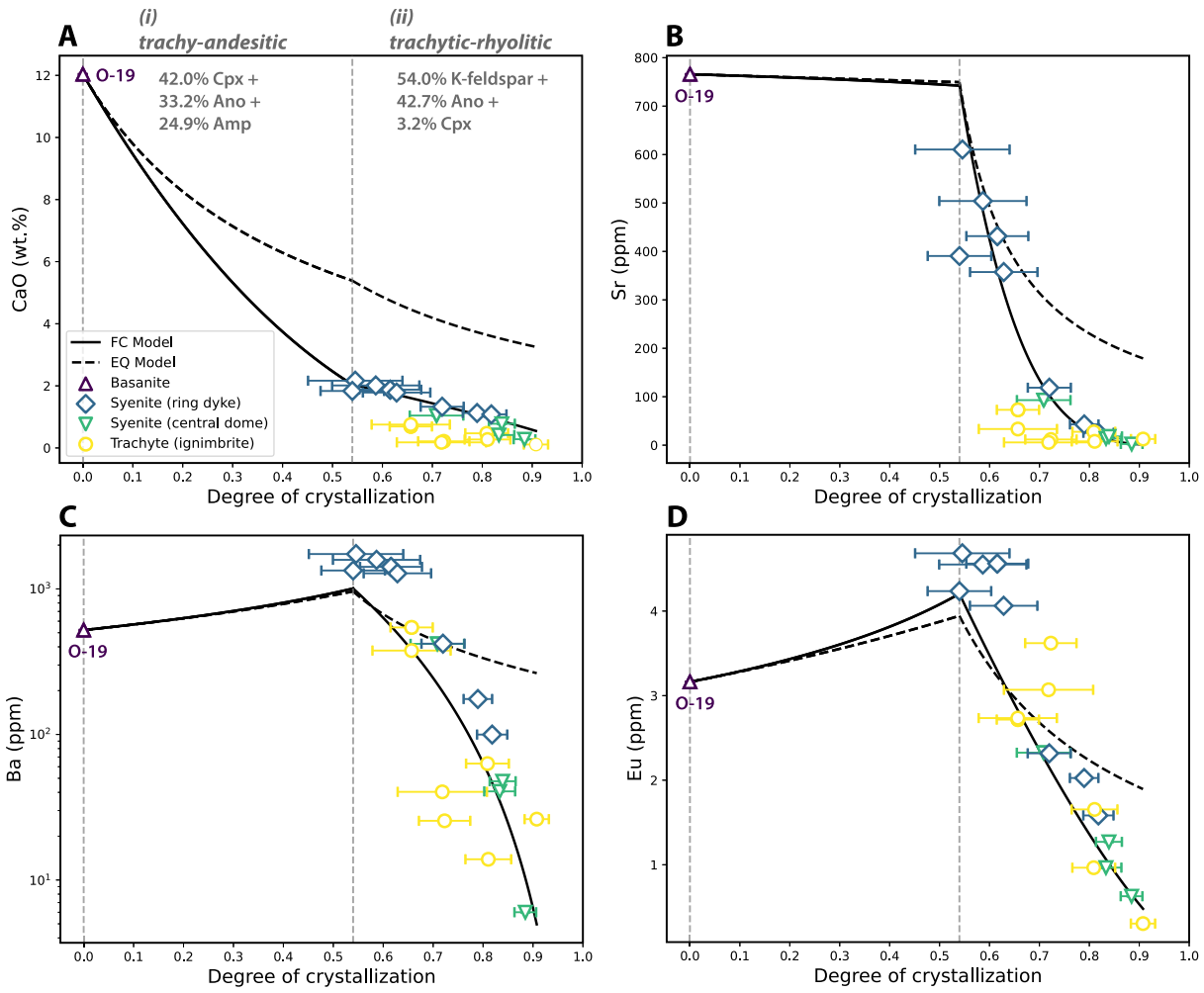

Fig. 3. Trace element variations and equilibrium and fractional crystallization modeling results. We use the evolved basanite O-19 for the parental magma composition. Mineral partition coefficients (D) for Sr, Ba, and Eu are from the Geochemical Earth Reference Model (GERM) Partition Coefficients Database (KdD) (https://kdd.earthref.org/KdD). Ano – anorthoclase; Amp – amphibole; Cpx – clinopyroxene. FC – fractional crystallization; EQ – equilibrium crystallization.

Using the calculated mineral proportions and mineral partition coefficients (Table S3, from the Geochemical Earth Reference Model Partition Coefficients Database, https://kdd.earthref.org/KdD), we modeled trace elemental variations of Sr, Ba, and Eu in the melt (Fig. 3 B–D). The modeled evolution of CaO is also plotted versus our data (Fig. 3A). Comparing data and modeling results yields remarkable agreement between the major and trace element systematics and our fractional crystallization model. In particular, the fractional crystallization modeling matches the characteristic depletions of Sr, Ba, and Eu up to extreme degrees of solidification (54–91%), which are all diagnostic features of feldspar fractionation. In addition, the extremely low concentrations of Sr, Ba, and Eu in the late stages of differentiation make them sensitive tracers of magma mixing. For example, the extensive depletion of Sr puts strong constraints on the extent of contamination as the possible contaminants have much higher Sr concentrations (∼250 ppm for the Precambrian basement and ∼700 ppm for the Cambrian to Silurian sediments) (Neumann et al., 1985). Contaminating the differentiating magma with these rocks would not reproduce the extremely-depleted Sr concentrations that are observed. Together, the consistent and systematic decrease in Sr, Ba, and Eu, especially for the main-series magma, precludes magma mixing during magma differentiation.

To further test open-system behavior, we have modeled elemental variations expected for open-magma crystallization (DePaolo, 1981) to compare with our data. The elemental variations of CaO (a representative compatible element) and Th (a representative incompatible element), including both the main-series syenites and trachytic–rhyolitic ignimbrites, agree best with the modeled closed-system crystallization (Fig. S8). The observed elemental variations also do not display the diagnostic features predicted for open-magma crystallization: limited depletion of compatible elements (such as Ca) and continuous enrichment in incompatible elements (such as Th) (O'Hara, 1977; DePaolo, 1981) (Fig. S8). Therefore, these comparisons conclude that the Øyangen samples document a very limited extent of magma replenishment during magma differentiation.

Within the felsic stage, trachytic–rhyolitic ignimbrites display a nuanced but discernable deviation from the evolution of syenites from ring dykes and central domes, manifesting in both major element (e.g., Na_2O, K_2O, CaO, MnO) and trace element (e.g., Sr, Ba) variations (Fig. 1B, Fig. 3). Also, the trachytic–rhyolitic ignimbrites generally have a larger spread in elemental concentrations. Such differences likely result from the complex source materials incorporated in the formation of eruptive ignimbrites, in contrast to the intrusive main series of magma.

In summary, major and trace element variations and modeling resolve a co-genetic fractional crystallization sequence recorded in the samples, of which feldspar dominates the late-stage Ca budget. Affirmation of the magmatic history enables us to directly probe Ca-isotope systematics during magmatic differentiation.

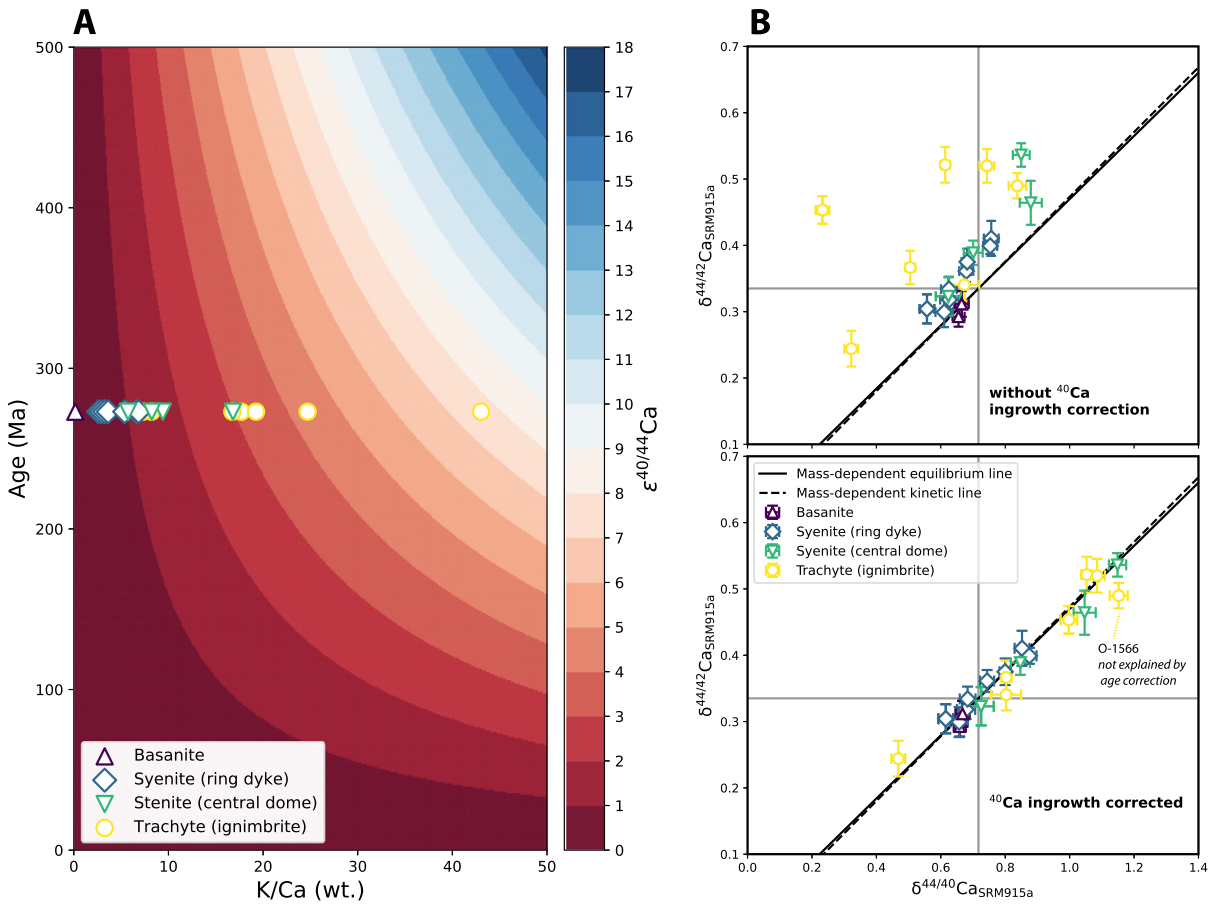

Fig. 4. Ca-isotope data and ^{40}K-^{40}Ca radiogenic ingrowth correction. (A) $\varepsilon^{40/44}$Ca as a function of K/Ca (wt.) and age of the rocks (ca. 273 Ma for the Øyangen Caldera). (B) $\delta^{44/42}$Ca vs. $\delta^{44/40}$Ca (relative to standard SRM915a) before and after age correction for ^{40}Ca ingrowth. After correction, only O-1566 does not fall along the theoretical mass fractionation lines, implying an isotope composition not accounted for by K-Ca age correction. The mass-dependent equilibrium line is defined by a slope of 2.0995^{-1}, while the kinetic line has a slope of 2.0483^{-1} (Young et al., 2002). The intercept of the horizontal and vertical grey lines shows the $\delta^{44/40}$Ca (0.717‰) and $\delta^{44/42}$Ca (0.335‰) values of CaIV-1 relative to SRM915a, which are close to the values of the analyzed igneous rocks.

5.2. Rayleigh (equilibrium) isotopic fractionation of the main-series samples

With the fractional crystallization sequence established above, we assess the mechanism for the observed Ca-isotope variations in our samples. The strong correlations between $\delta^{44/40}$Ca, CaO, and Eu/Eu* for the main-series syenite samples (Fig. 5) substantiate that the Ca-isotope changes are best explained by feldspar fractionation during crystallization. Weak to no correlations between $\delta^{44/40}$Ca, CaO, and Eu/Eu* of the trachytic–rhyolitic ignimbrites (Fig. 5) align with their complex petrogenetic origins. Thereby, the Ca isotope data of trachytic–rhyolitic ignimbrites are not prioritized for interpretations in the context of magmatic differentiation.

During magma crystallization, mass-dependent equilibrium and kinetic isotopic fractionation could both be important (Watson and Müller, 2009; Antonelli et al., 2019a and 2019b). Significant $\delta^{44/40}$Ca variations (up to ~0.2‰) within melt compositions have been mostly observed from volcanic units (Zhu et al., 2021). Fractionation greater than ~0.2‰ was mainly ascribed to kinetic isotopic effects via Ca diffusion during rapid feldspar growth (Antonelli et al., 2019b; Zhu et al., 2021). The main series of the Øyangen samples, consisting of intrusive syenites from ring dykes and central domes, displays a total $\delta^{44/40}$Ca change of ~0.53‰, so far, the largest systematic variations confirmed for a well-preserved magma series. Importantly, this is the first pronounced Ca-isotope variation discovered from a sequence of igneous intrusions instead of volcanics. Clarifying the fractionation mechanism of the Øyangen samples is vital for our fundamental understanding of Ca isotopic variability among diverse igneous origins and conditions, which ultimately defines the power of Ca-isotopes as a tracer of magmatic differentiation.

The slow crystallization rates of intrusive rocks are most compatible with fractionation closer to expected equilibrium (Watson and Müller, 2009; Antonelli et al., 2019a). This can be further tested by comparing our Ca-isotope data with the Rayleigh equilibrium fractionation model, which gives:

$$\delta^{44/40}Ca_{melt} = (1{,}000 + \delta_T^{44/40}Ca)\, f^{(\alpha^{44/40}Ca-1)} - 1{,}000 \qquad (6)$$

Expressing $\delta^{44/40}$Ca as a function of ln(F), equation (6) becomes:

$$\delta^{44/40}Ca_{melt} = \delta_T^{44/40}Ca + 1{,}000D\left(\alpha^{44/40}Ca - 1\right)\ln(F) \qquad (7)$$

where $\delta^{44/40}Ca_{melt}$ is the evolution of the Ca-isotope ratio in the melt; $\delta_T^{44/40}Ca$ is the initial isotopic composition; $f(=F^D)$ is the mass fraction of the reference isotope (^{40}Ca) in the melt; $\alpha^{44/40}$Ca is the bulk fractionation factor of the fractionating mineral assemblage [$\alpha^{44/40}\text{Ca} = (^{44}\text{Ca}/^{40}\text{Ca}_{\text{solid}})/(^{44}\text{Ca}/^{40}\text{Ca}_{\text{melt}})$]. The ^{44}Ca/^{40}Ca evolution of the instantaneous cumulates follows as:

$$\delta^{44/40}Ca_{cum} = \delta^{44/40}Ca_{melt} + 1{,}000\ln(\alpha^{44/40}Ca) \qquad (8)$$

Equation (7) expresses a linear relationship between $\delta^{44/40}Ca_{melt}$ and ln(F), whose slope is given by 1,000D(α-1). This approach can test whether Rayleigh fractionation describes the observed isotopic changes and allows for application of linear regression to define the best-fit bulk $\alpha^{44/40}$Ca.

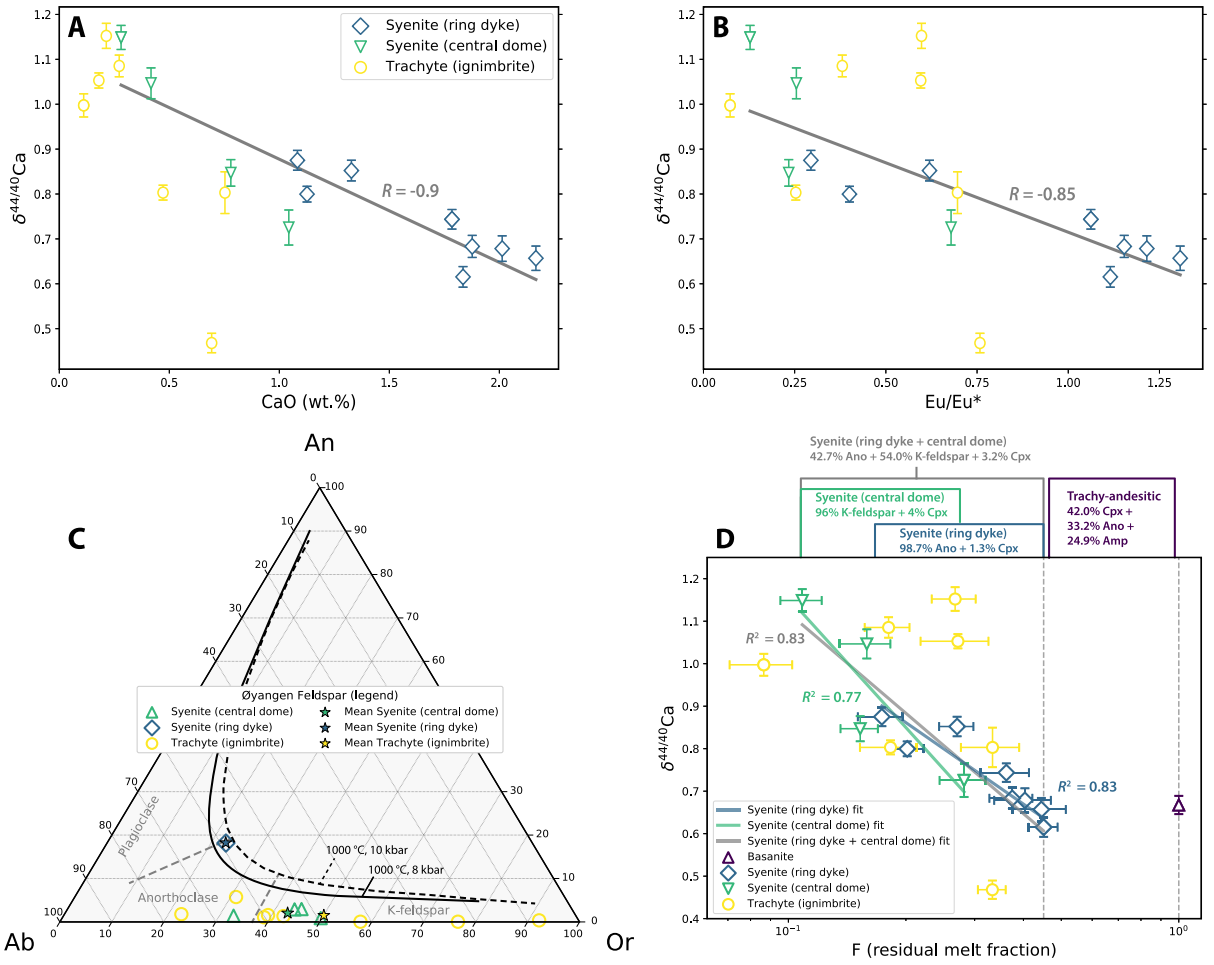

Fig. 5. Ca-isotope variations with feldspar fractionation. (A) & (B) $\delta^{44/40}$Ca vs. CaO (wt.%) and $\delta^{44/40}$Ca vs. Eu/Eu* for the felsic-stage magma. Correlation coefficients (R) are determined using the main-series syenite samples from ring dykes and central domes. (C) Anorthite (An) – Albite (Ab) – Orthoclase (Or) ternary diagram illustrating feldspar compositions for our samples. Curves show the calculated miscibility gaps for 1,000 °C following Yoshimura et al. (2008). The ca. 1,000 °C crystallization temperature for the anorthoclase in the syenites from ring dykes is broadly consistent with the MELTS calculation. (D) $\delta^{44/40}$Ca as a function of ln(F), where a linear relationship [slope = 1,000$D(\alpha - 1)$] is expected for Rayleigh isotopic fractionation (see text). The best-fit slopes yield bulk α, from which α of feldspar can be disentangled and estimated. Uncertainties on the data are two standard errors (2SE). Ano – anorthoclase; Amp – amphibole; Cpx – clinopyroxene.

We present measured $\delta^{44/40}$Ca versus ln(F) in Fig. 5D. Linear regressions yield high correlation coefficients ($R^2 = 0.83$, $N = 12$) for all main-series samples of the felsic stage, as well as for independent fittings for the syenites from ring dykes ($R^2 = 0.83$, $N = 8$) and the central dome samples ($R^2 = 0.77$, $N = 4$). This demonstrates that the Ca-isotope changes agree well with Rayleigh fractionation models throughout magma solidification. In more detail, we observe no systematic $\delta^{44/40}$Ca offset between the fine-grained syenites from central domes and coarse-grained syenites from ring dykes along the main evolution trend (Fig. 5D). This implies no discernable signatures of disequilibrium effects induced by variable rates of crystal precipitation, which otherwise could result in separate fractionation behaviors between the two types of melts. For instance, if kinetic effects played a considerable role during crystallization, the rapid-cooling central-dome syenites could have generated a systematic shift from the $\delta^{44/40}$Ca evolution of the slow-cooling ring-dyke syenites, assuming that the kinetic Ca-isotope fractionation is larger for faster crystallizing feldspar (Antonelli et al., 2019a). Therefore, the Ca-isotope results for the main series favor an equilibrium fractionation mechanism, although the possible involvement of minor kinetic effects cannot be excluded. The substantial deviations of the $\delta^{44/40}$Ca values of the trachytic–rhyolitic ignimbrites from the mean trend of the melt (Fig. 5D) might reflect the complex and heterogeneous nature of their building materials.

5.3. Isotopic fractionation factors and Ca-isotope evolution

Considering that, for systems defined by Rayleigh fractionation, the slope in a plot of $\delta^{44/40}$Ca versus ln(F) equals 1,000$D(\alpha$-1), inversion of the slopes can yield accurate estimations of bulk $\alpha^{44/40}$Ca. Using a weighted-least-squares method (Williamson, 1968), we compute the best-fit slopes for (1) the syenite samples from ring dykes, (2) the syenite samples from central domes, and (3) the entire felsic stage containing both sample types. A significant difference is resolved between the slopes of the ring dyke samples and the central dome samples (Fig. 5D), suggesting considerable changes in bulk $\alpha^{44/40}$Ca with the varying mineral compositions and proportions. We take the mean temperature for each crystallizing assemblage to account for the temperature-dependence of fractionation factors [$\alpha - 1 \sim (1/T)^2$] (e.g., the mean T is 1,217 K for the syenite samples from ring dykes that span between 1,151 K to 1,284 K) (Fig. 2D) (Table 1). The corresponding bulk $\alpha^{44/40}$Ca at 1,000 K, a reference temperature, is then calculated from $\alpha^{44/40}Ca_{(T)}$ using:

$$\alpha^{44/40}Ca_{(T)} - 1 = (\alpha^{44/40}Ca_{(1{,}000)} - 1)/\left(\frac{T}{1{,}000}\right)^2 \quad (9)$$

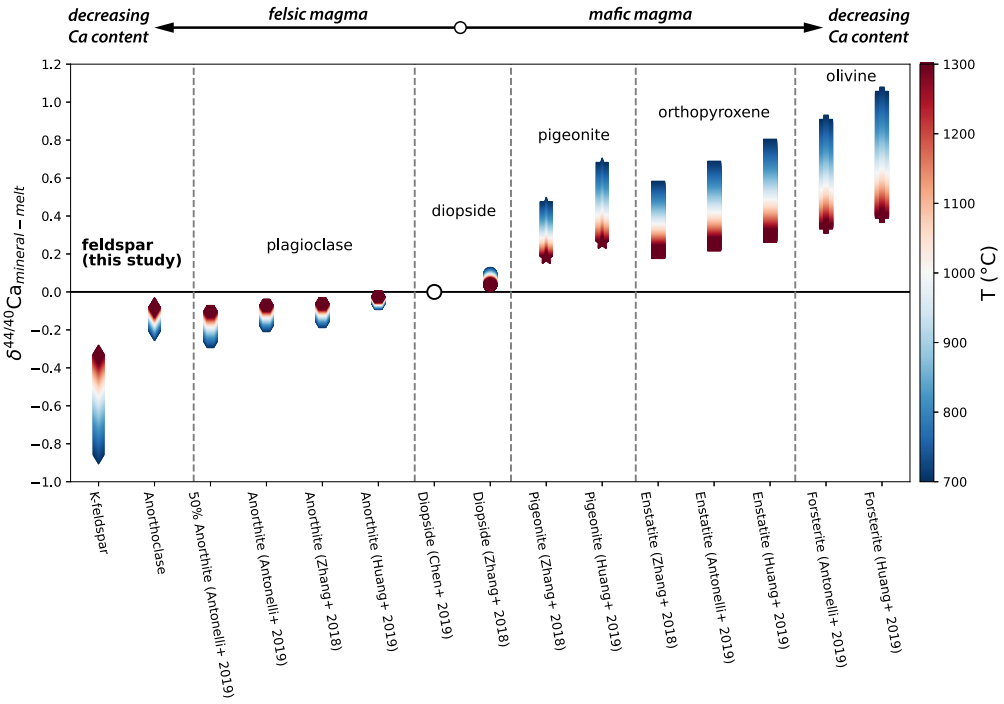

Fig. 6. Compilation of mineral–melt $^{44}Ca/^{40}Ca$ isotopic fractionation factors of major rock-forming minerals in the Earth's crust, determined in this study and from the literature.

Because diopside is the only major Ca-bearing mineral other than feldspar in both the ring-dyke and central-dome syenite samples, we can determine the $\alpha^{44/40}Ca$ for feldspar by subtracting the contribution of $\alpha^{44/40}Ca_{diopside-melt}$ from the bulk $\alpha^{44/40}Ca$. Adopting $\alpha^{44/40}Ca_{diopside-melt} = 1.00009 \pm 0.00007$ at 1,000 K from Zhang et al. (2018), $\alpha^{44/40}Ca_{anorthoclase-melt}$ and $\alpha^{44/40}Ca_{K\text{-}feldspar-melt}$ are disentangled from the ring dyke and central dome samples, respectively (for results see Table 2) (Supplementary Material: Section 6). Our calculated mineral-melt fractionation factor for the whole felsic stage, 0.999713 ± 0.000036 (two standard errors) (Table S3), agrees within error with the mineral-melt fractionation factor obtained by the regression method (0.999718 ± 0.000039), demonstrating the consistency of the $\alpha^{44/40}Ca_{mineral-melt}$ estimates.

We synthesized the $\alpha^{44/40}Ca$ estimations for feldspar determined in our study with those for major rock-forming minerals of Earth's crust from the literature (Fig. 6, Table 2). We expressed the $^{44}Ca/^{40}Ca$ fractionation between minerals and melts as $\delta^{44/40}Ca_{mineral-melt} = 1{,}000(\alpha^{44/40}Ca_{mineral-melt} - 1)$. Inter-mineral fractionation originally reported as $\delta^{44/40}Ca_{mineral-diopside}$ from the literature are converted to $\delta^{44/40}Ca_{mineral-melt}$ assuming $\delta^{44/40}Ca_{diopside-melt} = 0.09 \pm 0.07‰$ (Zhang et al., 2018). $\delta^{44/40}Ca_{anorthoclase-melt}$ from our study exhibits similar fractionation effects to plagioclase. K-feldspar reveals the most negative $\delta^{44/40}Ca$ value relative to the melt discovered so far (−0.81 ± 0.10‰ at 1,000 K). Ca-isotope analyses of mineral phenocrysts (Antonelli et al., 2019a) also imply that K-feldspar may have the lightest Ca-isotope signature among common rock-forming minerals (up to $\delta^{44/40}Ca = -2‰$ relative to BSE), broadly consistent with our results. An overall trend shows that more Ca-depleted minerals bear larger fractionation effects (Fig. 6). Such a Ca-concentration effect has been predicted by experiments and first-principles calculations for minerals mainly with positive $\delta^{44/40}Ca_{mineral-diopside}$, including olivine, orthopyroxene, pigeonite, and garnet (Feng et al., 2014; Wang et al., 2017; Huang et al., 2019; Li et al., 2022). This is primarily an artifact of the length of the Ca-O bond, where heavy Ca-isotopes (e.g., ^{44}Ca) have a preference for shorter, stiffer bonds. Substituting Ca into crystal lattices generally increases the length of the Ca-O bond, leading to less-pronounced fractionations between minerals and melt for minerals enriched in Ca (e.g., Feng et al., 2014; Wang et al., 2017; Huang et al., 2019; Antonelli and Simon, 2020; Li et al., 2022). A possible Ca-concentration effect has been postulated for feldspar with negative $\delta^{44/40}Ca_{mineral-diopside}$ from first-principles estimates (lighter $^{44}Ca/^{40}Ca$ with decreasing anorthite content, Antonelli et al., 2019a); our data provide the first evidence for this effect in a continuous natural magma sequence.

We reconstruct the Ca-isotope evolution of the Øyangen Caldera using Rayleigh fractionation [equation (6) & (8)], accounting for propagated errors surrounding the initial isotopic composition (sample O-19) and temperature-dependent fractionation factors with a Monte Carlo model that we developed (Supplementary Material: Section 7) (Fig. 7, Table S3). We implemented Monte Carlo modeling for (1) measured $\delta^{44/40}Ca$ (corrected for ingrowth of radiogenic ^{40}Ca) (Fig. 7 A) and (2) $\delta^{44/40}Ca$ calculated from measured $\delta^{44/42}Ca$, assuming a mass-dependent fractionation relationship ($\delta^{44/40}Ca \approx 2.0483 * \delta^{44/42}Ca$, Young et al., 2002) (Fig. 7B). Both models yield similar results (Fig. 7). The $\delta^{44/40}Ca$ value of the parental magma (0.67 ± 0.02‰) is similar to the typically low average $\delta^{44/40}Ca$ values of alkaline igneous rocks including ocean island basalts (from ~0.70‰ to ~0.85‰) (Eriksen and Jacobsen, 2022). Forward modeling of $\delta^{44/40}Ca$ yields high correspondence with the observed Ca-isotope variability throughout the whole sequence (Fig. 7). Most of the main-series syenite samples and part of the trachytic–rhyolitic ignimbrites overlap the modeled melt curve within the 95% confidence envelope.

Our data and modeling corroborate that no discernable $\delta^{44/40}Ca$ fractionation (< 0.05‰) is expected in an intermediate crystallization sequence, as the isotopic effects of mafic minerals (including clinopyroxene and amphibole) and feldspar nearly cancel out each other. This is consistent with Ca-isotope measurements from the basalt to dacite sequence in the Kilauea Iki lava lake, Hawaii (<0.07‰ change, Zhang et al., 2018) and from the basaltic andesite to andesite in the eastern Manus Basin (Zhu et al., 2021). Throughout the felsic stage, the ~0.53‰ $\delta^{44/40}Ca$ fractionation

Table 2
Ca isotopic fractionation factors for rock-forming minerals of Earth's crust.

Mineral	$\delta^{44/40}Ca_{mineral\text{-}melt}$	2SE (2SD)	$\alpha^{44/40}Ca_{mineral\text{-}melt}$	Methods	References
Feldspar					
K-feldspar	−0.81	0.10	0.999187	Data regression	**This study**
Anothoclase	−0.20	0.04	0.999803	Data regression	**This study**
50% Anorthite	−0.25	-	0.999750	First-principles calculation	Antonelli et al. (2019a)
Anorthite	−0.17	-	0.999830	First-principles calculation	Antonelli et al. (2019a)
Anorthite	−0.15	0.08	0.999850	Data regression	Zhang et al. (2018)
Anorthite	−0.06	-	0.999940	First-principles calculation	Huang et al. (2019)
Clinopyroxene					
Diopside	0	-	1.000000	Data interpretation	Chen et al. (2019)
Diopside	0.09	0.07	1.000090	Data regression	Zhang et al. (2018)
Pigeonite	0.44	0.13	1.000440	Data regression	Zhang et al. (2018)
Pigeonite	0.64	-	1.000636	First-principles calculation	Huang et al. (2019)
Orthopyroxene					
Enstatite	0.52	0.1	1.000520	Data regression	Zhang et al. (2018)
Enstatite	0.62	-	1.000620	First-principles calculation	Antonelli et al. (2019a)
Enstatite	0.73	-	1.000730	First-principles calculation	Huang et al. (2019)
Olivine					
Forsterite	0.85	-	1.000850	First-principles calculation	Antonelli et al. (2019a)
Forsterite	0.99	-	1.000990	First-principles calculation	Huang et al. (2019)

Notes: Isotopic fractionation effects are determined for 1,000 K.
2SE/2SD – two standard errors/deviations of $\delta^{44/40}Ca_{mineral\text{-}melt}$.

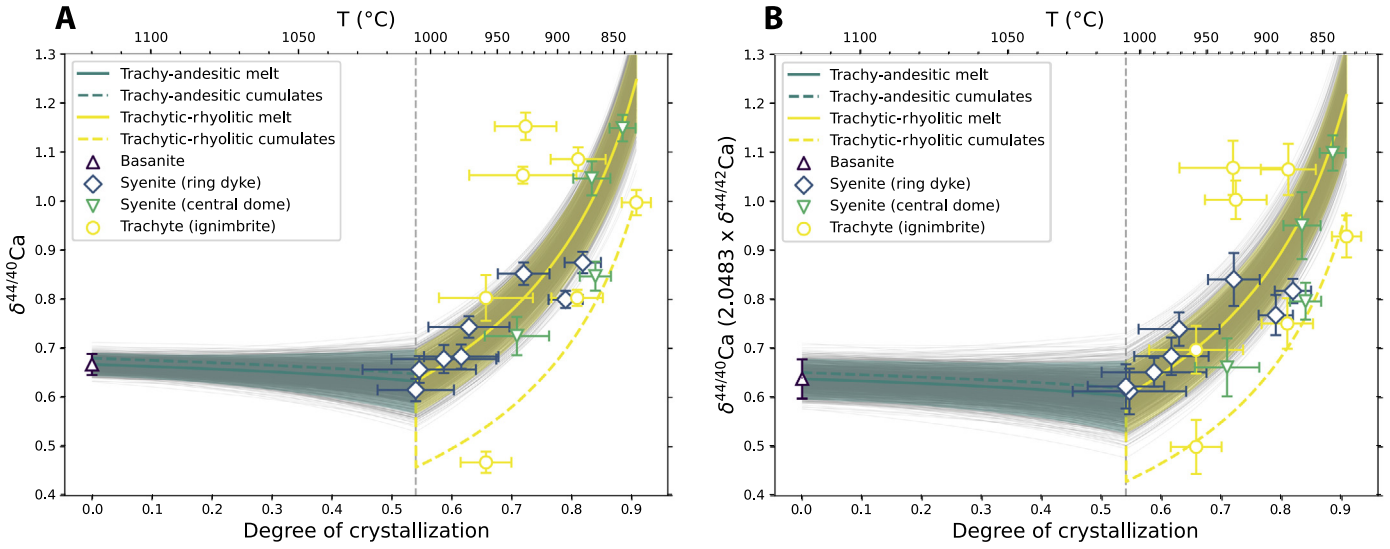

Fig. 7. Ca-isotope evolution of the Øyangen Caldera. (A) & (B) $\delta^{44/40}$Ca vs. degree of crystallization. $\delta^{44/40}$Ca in (A) are after correction for ^{40}Ca radiogenic ingrowth; $\delta^{44/40}$Ca in (B) are calculated from $\delta^{44/42}$Ca assuming a theoretical mass-dependent fractionation relationship. Isotopic evolution is modeled using Rayleigh fractionation with a Monte Carlo approach (Supplementary Material: Section 7). For clarity of the figure, fine grey curves show the first 2,000 times out of all 10,000 simulations. Colored solid and dashed curves represent the mean $\delta^{44/40}$Ca compositions of the melt and cumulates, respectively. Colored fields bound the 95% confidence intervals of our melt model. Uncertainties on the Ca-isotope data are two standard errors (2SE). (For interpretation of the colors in the figure(s), the reader is referred to the web version of this article.)

found in both the intrusions and the volcanics highlights the capacity of Ca-isotopes as a sensitive tracer of igneous fractionation, calling for tests in other magma types and tectonic environments. The discoveries invoke new applications of Ca isotopes in diverse topics surrounding magmatic history at various spatial and temporal scales.

5.4. Implications for planetary differentiation

Recognizing the prominent feldspar isotopic effects augments the application of Ca-isotopes in studying planet-scale differentiation. Recently, progress has been made in modeling the Ca-isotope evolution throughout the crystallization of the early lunar magma ocean (LMO). Modeling has predicted a decrease in $\delta^{44/40}$Ca in the first ~80% of the LMO solidification dominated by olivine and orthopyroxene, followed by an increase in the late stages (~0.05‰) controlled by plagioclase, clinopyroxene, and orthopyroxene (Huang et al., 2019). Using a similar LMO crystallization model and the same set of inter-mineral fractionation factors, however, Klaver et al. (2021) modeled monotonically decreasing $\delta^{44/40}$Ca throughout the LMO crystallization. Conflicting results trace two primary causes. First, a systematic offset between their assumptions of mineral-melt fractionations — Huang et al. (2019) assumed $\delta^{44/40}Ca_{diopside\text{-}melt} = 0 \pm 0.05$‰ and Klaver et al. (2021) used $\delta^{44/40}Ca_{diopside\text{-}melt} = 0.09 \pm 0.07$‰ following Zhang et al. (2018). Second, use of a comparatively small $\delta^{44/40}Ca_{plagioclase\text{-}diopside}$ (−0.15‰ at 1,000 K) in both studies. Our resolved $\delta^{44/40}Ca_{anorthoclase\text{-}diopside}$ agrees better with the $\delta^{44/40}Ca_{anorthite\text{-}diopside}$ estimated from Zhang et al. (2018) and Antonelli et al. (2019a) (Table 2), which collectively suggests a value ranging from −0.34‰ to −0.24‰ (at 1,000 K), a more probable estimation for $\delta^{44/40}Ca_{plagioclase\text{-}diopside}$. Using this larger $\delta^{44/40}Ca_{plagioclase\text{-}diopside}$ would alleviate the discrepancy between

models under mildly different assumptions of mineral-melt fractionation. Additionally, the more negative $\delta^{44/40}Ca_{plagioclase-melt}$ predicts greater variations in $\delta^{44/40}Ca$ of the LMO approaching its final crystallization and larger fractionation between the magma, sinking cumulates, and the floating anorthite crust, a prediction that is testable in subsequent investigations.

Although relatively new to the application of planetary differentiation, Ca-isotopes carry a unique advantage and potential. Other non-traditional stable isotope systematics, including K, Mg, Si, and Fe, are slightly volatile to moderately volatile and prone to accretional and impact vapor loss during planet formation (Wang et al., 2015; Wang and Jacobsen, 2016; Hin et al., 2017). Such processes could have overprinted the primary stable isotopic composition since magma crystallization, making it challenging to clarify the magmatic effects and conclude unambiguous inferences. As one of the most refractory elements, Ca is resistant to evaporative loss and therefore preserves mostly the initial magmatic signals. Boosted by the discovery of notable isotopic fractionation during magmatic differentiation, Ca-isotopes are projected to serve as a powerful technique in reconstructing the crustal evolution of differentiated planetary bodies beyond the Earth-moon system, including Mars and Vesta, when coupled with other isotope systems (Elkins-Tanton, 2012; Schiller et al., 2011, 2017; Sedaghatpour and Jacobsen, 2019).

6. Conclusions

We report high-precision Ca-isotope measurements for the late-Permian alkaline igneous suite in the Øyangen Caldera, Oslo Rift, Norway. Major and trace element variations demonstrate a cogenetic closed-system fractional crystallization sequence of the main-series samples, including basanites, ring-dyke syenites, and central-dome syenites. We observe an indiscernible change in $\delta^{44/40}Ca$ ($< 0.05‰$) from the basanite to the primitive ring-dyke syenites in the intermediate magma and a remarkable increase in $\delta^{44/40}Ca$ ($\sim 0.53‰$) among the evolved ring-dyke and central-dome syenites in the felsic magma. The rise in $\delta^{44/40}Ca$ is most consistent with equilibrium isotopic fractionation controlled by feldspar during fractional crystallization. Using a regression approach, we constrain the $^{44}Ca/^{40}Ca$ fractionation factors for plagioclase and K-feldspar facilitated by high precision Ca-isotope data. Integrated with a mineral fractionation factor database, the new results reveal a general inverse correlation between Ca concentration and extent of fractionation. K-feldspar carries the lightest $^{44}Ca/^{40}Ca$ among the major rock-forming minerals of Earth's crust. Confirmation of substantial fractionation during magma solidification promotes the utilization of Ca-isotopes in probing the history of igneous differentiation in versatile scopes, from the evolution of a single magma chamber to hypothesized global magma oceans.

CRediT authorship contribution statement

H.F., S.B.J. and B.T.L. conceptualized and initiated the project. H.F. performed analytical work, developed the interpretation with input from S.B.J. and Z.T.E. and wrote the manuscript. All authors reviewed and edited the manuscript to improve it. Z.T.E. provided Ca-isotope data for rock standards. B.T.L. provided samples and geological context, elemental data for mineral separates as well preliminary data to show that this caldera was the perfect place for this project. All authors discussed ideas and provided comments throughout the investigation.

Declaration of competing interest

The authors declare that they have no known competing financial interests or personal relationships that could have appeared to influence the work reported in this paper.

Acknowledgements

We thank Yvan Gérard and Chris Parendo for helpful assistance in maintaining the Nu Sapphire (SP001) mass spectrometer. We thank Mingzhen Yu for performing the MELTS calculations. We thank Rajdeep Dasgupta for careful editorial handling. Finally, we are thankful to Scott Angus MacLennan and an anonymous reviewer for constructive comments. This work was partly supported by the DOE grant #DE-NA0003904 (the NNSA SSAA program) and NASA Emerging Worlds Program grant #80NSSC20K0346, both to S.B.J.

Appendix A. Supplementary material

Supplementary material related to this article can be found online at https://doi.org/10.1016/j.epsl.2022.117743.

References

Allègre, C.J., Treuil, M., Minster, J.-F., Minster, B., Albarède, F., 1977. Systematic use of trace element in igneous process. Contrib. Mineral. Petrol. 60, 57–75.
Amsellem, E., Moynier, F., Bertrand, H., Bouyon, A., Mata, J., Tappe, S., Day, J.M.D., 2020. Calcium isotopic evidence for the mantle sources of carbonatites. Sci. Adv. 6, eaba3269.
Antonelli, M.A., Schiller, M., Schauble, E.A., Mittal, T., DePaolo, D.J., Chacko, T., Grew, E.S., Tripoli, B., 2019a. Kinetic and equilibrium Ca isotope effects in high-T rocks and minerals. Earth Planet. Sci. Lett. 517, 71–82.
Antonelli, M.A., Mittal, T., McCarthy, A., Tripoli, B.A., Watkins, J., DePaolo, D.J., 2019b. Ca isotopes record rapid crystal growth in volcanic and subvolcanic systems. Proc. Natl. Acad. Sci. 116, 20315–20321.
Antonelli, M.A., Simon, J.I., 2020. Calcium isotopes in high-temperature terrestrial processes. Chem. Geol. 548, 119–651.
Brewer, A.W., Teng, F-Z., Mullen, E., 2018. Magnesium isotopes as a tracer of crustal materials in volcanic arc magmas in the Northern Cascade Arc. Front. Earth Sci. 6 (21).
Cashman, K., Giordano, G., 2014. Calderas and magma reservoirs. J. Volcanol. Geotherm. Res. 288, 28–45.
Chen, C., Dai, W., Wang, Z., Liu, Y., Li, M., Becker, H., Foley, S.F., 2019. Calcium isotope fractionation during magmatic processes in the upper mantle. Geochim. Cosmochim. Acta 249, 121–137.
Corfu, F., Dahlgren, S., 2008. Perovskite U–Pb ages and the Pb isotopic composition of alkaline volcanism initiating the Permo-Carboniferous Oslo Rift. Earth Planet. Sci. Lett., 256–269.
Corfu, F., Larsen, B.T., 2020. U-Pb systematics in volcanic and plutonic rocks of the Krokskogen area: resolving a 40 million years long evolution in the Oslo Rift. Lithos, 376–377.
DePaolo, D.J., 1981. Trace element and isotopic effects of combined wallrock assimilation and fractional crystallization. Earth Planet. Sci. Lett. 53, 189–202.
Elkins-Tanton, L.T., 2012. Magma oceans in the inner solar system. Annu. Rev. Earth Planet. Sci. 40, 113–139.
Eriksen, Z.T., Jacobsen, S.B., 2022. Calcium isotope constraints on OIB and MORB petrogenesis: the importance of melt mixing. Earth Planet. Sci. Lett. 593, 117665.
Feng, C., Qin, T., Huang, S., Wu, Z., Huang, F., 2014. First-principles investigations of equilibrium calcium isotope fractionation between clinopyroxene and Ca-doped orthopyroxene. Geochim. Cosmochim. Acta 143, 132–142.
Feng, L., Zhou, L., Yang, L., Zhang, W., Wang, Q., Shuoyun, T., Hu, Z., 2018. A rapid and simple single-stage method for Ca separation from geological and biological samples for isotopic analysis by MC-ICP-MS. J. Anal. At. Spectrom. 33, 413–421.
Gavrilenko, M., Ozerov, A.Y., Kyle, P.R., Carr, M.J., Nikulin, A., Vidito, C., Danyushevsky, L., 2016. Abrupt transition from fractional crystallization to magma mixing at Gorely volcano (Kamchatka) after caldera collapse. Bull. Volcanol. 78, 1–28.
Gualda, G.A.R., Ghiorso, M.S., Lemons, R.V., Carley, T.L., 2012. Rhyolite-MELTS: a modified calibration of MELTS optimized for silica-rich, fluid-bearing magmatic systems. J. Petrol. 53, 875–890.
Hin, R.C., Coath, C.D., Carter, P.J., Nimmo, F., Lai, Y., Pogge von Strandmann, P.A., Willbold, M., Leinhardt, Z.M., Walter, M.J., Elliott, T., 2017. Magnesium isotope evidence that accretional vapour loss shapes planetary compositions. Nature 549, 511–515.
Huang, F., Zhou, C., Wang, W., Kang, J., Wu, Z., 2019. First- principles calculations of equilibrium Ca isotope fractionation: Implication for oldhamite formation and evolution of lunar magma ocean. Earth Planet. Sci. Lett. 510, 153–160.
Huang, S., Farkaš, J., Jacobsen, S.B., 2010. Calcium isotopic fractionation between clinopyroxene and orthopyroxene from mantle peridotites. Earth Planet. Sci. Lett. 292, 337–344.
Huang, S., Farkaš, J., Jacobsen, S.B., 2011. Stable calcium isotopic compositions of Hawaiian shield lavas: evidence for recycling of ancient marine carbonates into the mantle. Geochim. Cosmochim. Acta 75, 4987–4997.

Johnson, C.M., Beard, B.L., Albarède, F., 2004. Overview and general concepts. Rev. Mineral. Geochem. 55, 1–24.
Klaver, M., Luu, T.H., Lewis, J., Jansen, M.N., Anand, M., Schwieters, J.B., Elliott, T., 2021. The Ca isotope composition of mare basalts as a probe into the heterogeneous lunar mantle. Earth Planet. Sci. Lett. 570, 117079.
Kang, J.-T., Ionov, D.A., Liu, F., Zhang, C.-L., Golovin, A.V., Qin, L.-P., Zhang, Z.-F., Huang, F., 2017. Calcium isotopic fractionation in mantle peridotites by melting and metasomatism and Ca isotope composition of the Bulk Silicate Earth. Earth Planet. Sci. Lett. 474, 128–137.
Larsen, B.T., Olaussen, S., Sundvoll, B., Heeremans, M., 2008. The Permo-Carboniferous Oslo Rift through six stages and 65 million years. Episodes 31, 52–58.
Lamminen, J., Andersen, T., Nystuen, J.P., 2011. Zircon U-Pb ages and Lu-Hf isotopes from basement rocks associated with Neoproterozoic sedimentary successions in the Sparagmite Region and adjacent areas, South Norway: the crustal architecture of western Baltica. Nor. Geol. Tidsskr. 91, 35–55.
Li, Y., Wu, Z., Huang, S., Wang, W., 2022. Pressure and concentration effects on intermineral calcium isotope fractionation involving garnet. Chem. Geol. 591, 120–722.
McDonough, W.F., Sun, S.-S., 1995. The composition of the Earth. Chem. Geol. 120, 223–253.
Neumann, E.-R., Larsen, B.T., Sundvoll, B., 1985. Compositional variations among gabbroic intrusions in the Oslo rift. Lithos 18, 35–59.
Neumann, E.-R., Olsen, K.H., Baldridge, W.S., Sundvoll, B., 1992. The Oslo Rift: a review. Tectonophysics 208, 1–18.
Neumann, E.-R., Wilson, M., Heeremans, M., Spencer, E.A., Obst, K., Timmerman, M.J., Kirstein, L., 2004. Carboniferous-Permian rifting and magmatism in southern Scandinavia, the North Sea and northern Germany: a review. Geol. Soc. (Lond.) Spec. Publ. 223, 11–40.
O'Hara, M.J., 1977. Geochemical evolution during fractional crystallization of a periodically refilled magma chamber. Nature 266, 503–507.
Russell, W., Papanastassiou, D.A., Tombrello, T.A., 1978. Ca isotope fractionation on the Earth and other solar system materials. Geochim. Cosmochim. Acta 42, 1075–1090.
Sedaghatpour, F., Jacobsen, S.B., 2019. Magnesium stable isotopes support the lunar magma ocean cumulate remelting model for mare basalts. Proc. Natl. Acad. Sci. 116, 73–78.
Schiller, M., Baker, J.A., Creech, J., Paton, C., Millet, M.-A., Irving, A., Bizzarro, M., 2011. Rapid timescales for magma ocean crystallisation on the howardite–eucrite–diogenite parent body. Astrophys. J. 740, L22.
Schiller, M., Dallas, J., Creech, J., Bizzarro, M., Baker, J., 2017. Tracking the formation of magma oceans in the Solar System using stable magnesium isotopes. Geochem. Perspect. Lett. 3, 22–31.
Sun, J., Zhu, X.-K., Belshaw, N.S., Chen, W., Doroshkevich, A.G., Luo, W.-J., Song, W.-L., Chen, B.-B., Cheng, Z.-G., Li, Z.-H., Wang, Y., Kynicky, J., Henderson, G.M., 2021. Ca isotope systematics of carbonatites: insights into carbonatite source and evolution. Geochem. Perspect. Lett. 17, 11–15.
Tera, F., Eugster, O., Burnett, D.S., Wasserburg, G.J., 1970. Comparative study of Li, Na, K, Rb, Cs, Ca, Sr and Ba abundances in achondrites and in Apollo 11 lunar samples. In: Proceedings of the Apollo 11 Lunar Science Conference, Vol. 2, pp. 1637–1657.
Teng, F., Dauphas, N., Watkins, J., 2017. Non-traditional stable isotopes: retrospective and prospective. Rev. Mineral. Geochem. 82, 1–26.
Valdes, M.C., Debaille, V., Berger, J., Armytage, R.M.G., 2019. The effects of high-temperature fractional crystallization on calcium isotopic composition. Chem. Geol. 509, 77–91.
Wang (王阳), Y., He, Y., Wu, H., Zhu, C., Huang, S., Huang, J., 2019. Calcium isotope fractionation during crustal melting and magma differentiation: granitoid and mineral-pair perspectives. Geochim. Cosmochim. Acta 259, 37–52.
Watson, E.B., Müller, T., 2009. Non-equilibrium isotopic and elemental fractionation during diffusion-controlled crystal growth under static and dynamic conditions. Chem. Geol. 267, 111–124.
Wang, K., Jacobsen, S.B., Sedaghatpour, F., Chen, H., Korotev, R.L., 2015. The earliest Lunar Magma Ocean differentiation recorded in Fe isotopes. Earth Planet. Sci. Lett. 430, 202–208.
Wang, K., Jacobsen, S.B., 2016. Potassium isotopic evidence for a high-energy giant impact origin of the Moon. Nature 538, 487–490.
Wang, W.-Z., Qin, T., Zhou, C., Huang, S., Wu, Z., Huang, F., 2017. Concentration effect on equilibrium fractionation of Mg–Ca isotopes in carbonate miner- als: insights from first-principles calculations. Geochim. Cosmochim. Acta 208, 185–197.
Williamson, J., 1968. Least-squares fitting of a straight line. Can. J. Phys. 46, 1845–1847.
Wright, T.L., Doherty, P.C., 1970. A linear programming and least squares computer method for solving petrologic mixing problems. Geol. Soc. Am. Bull. 81, 1995–2008.
Yoshimura, Y., Motoyoshi, Y., Miyamoto, T., 2008. Sapphirine+quartz association in garnet: implication for ultrahigh-temperature metamorphism at Rundvågshetta, Lützow-Holm Complex, East Antarctica. Geol. Soc. (Lond.) Spec. Publ. 308, 377–390.
Young, E.D., Galy, A., Nagahara, H., 2002. Kinetic and equilibrium mass-dependent isotope fractionation laws in nature and their geochemical and cosmochemical significance. Geochim. Cosmochim. Acta 66, 1095–1104.
Zhang, H., Wang, Y., He, Y., Teng, F.-Z., Jacobsen, S.B., Helz, R.T., Marsh, B.D., Huang, S., 2018. No measurable calcium isotopic fractionation during crystallization of Kilauea Iki Lava Lake. Geochem. Geophys. Geosyst. 19, 3128–3131.
Zhu, H., Liao, R., Liu, H., Du, L., Li, H., Li, C., Zhang, Z., Sun, W., 2021. Calcium isotopic fractionation during magma differentiation: constraints from volcanic glasses from the eastern Manus Basin. Geochim. Cosmochim. Acta 305, 228–242.